Disentanglement of local field potential sources by independent component analysis

Valeri A. Makarov · Julia Makarova · Oscar Herreras

Abstract The spontaneous activity of working neurons yields synaptic currents that mix up in the volume conductor. This activity is picked up by intracerebral recording electrodes as local field potentials (LFPs), but their separation into original informative sources is an unresolved problem. Assuming that synaptic currents have stationary placing we implemented independent component model for blind source separation of LFPs in the hippocampal CA1 region. After suppressing contaminating sources from adjacent regions we obtained three main local LFP generators. The specificity of the information contained in isolated generators is much higher than in raw potentials as revealed by stronger phase-spike correlation with local putative interneurons. The spatial distribution of the population synaptic input corresponding to each isolated generator was disclosed by current-source density analysis of spatial weights. The found generators match with axonal terminal fields from subtypes of local interneurons and associational fibers from nearby subfields. The found distributions of synaptic currents were employed in a computational model to reconstruct spontaneous LFPs. The phase-spike correlations of simulated units and LFPs show laminar dependency that reflects the nature and magnitude of the synaptic currents in the targeted pyramidal cells. We propose that each isolated generator captures the synaptic activity driven by a different neuron subpopulation. This offers experimentally justified model of local circuits creating extracellular potential, which involves distinct neuron subtypes.

Keywords Blind source separation · Independent component analysis · Local field potentials · Neural sources · Model EEG · Hippocampus

1 Introduction

Neural information processing resides in the coordinated activity of multiple neuron subpopulations forming a complex system of local circuits and global networks. The activity of working neurons can be globally picked up by the electroencephalogram (EEG), a macroscopic variable mainly raised by the extracellular spatiotemporal summation of synaptic currents and recorded from the scalp by volume conduction. The mixing of electrical sources from different spatial origin is a major handicap for the study of brain signals at this level. So far the separation of the electrical activity of converging neuron populations into original informative sources is an unresolved problem (Mitzdorf 1985; Nunez and Srinivasan 2006). In its most general formulation it can be considered in the framework of the blind source separation paradigm.

Independent component analysis (ICA), as a class of methods for blind separation of data into underlying informational components, has matured in the last decade (for review see Choi et al. 2005). ICA has been used in

V. A. Makarov
Department of Applied Mathematics, Faculty of Mathematics,
Av. Complutense s/n, Univ. Complutense,
Madrid 28040, Spain

J. Makarova · O. Herreras (✉)
Department of Systems Neuroscience, Cajal Institute – CSIC,
Av. Doctor Arce 37,
Madrid 28002, Spain
e-mail: herreras@cajal.csic.es

surface electroencephalography to identify and separate coherent activity in groups of adjacent electrodes (see, e.g., Bell and Sejnowski 1995; Makeig et al. 2004; Jung et al. 2005; Castellanos and Makarov 2006). However, the heterogeneous electrical properties of the conducting medium, spatial cancellation and frequency scaling of currents in the volume conductor (López-Aguado et al. 2001; Bédard et al. 2004; Makarova et al. 2008) limit its utility to the gross localization of large electrical sources of unknown cellular origin. These restrictive factors are less relevant in intracerebral local field potential (LFP) studies (Tanskanen et al. 2005). Though, even LFPs are contributed by the multiple neurons involved in local and extrinsic circuits whose termination fields are near the recording electrode and may overlap extensively. None of the standard analysis techniques, e.g., spectral decomposition or current source density (CSD) analysis of raw LFPs can satisfactorily separate and localize different cellular generators of LFPs.

More recent approaches based on coherence analysis (Kocsis et al. 1999; Montgomery et al. 2009), principal component analysis or laminar population analysis (Einevoll et al. 2007) have been proven to be useful for separating important features of mixed deep electrical sources. In theory, if we assume that brain electrical sources are spatially stationary (i.e., immobile), then their best extraction from LFPs should be obtained within the ICA framework. Apart from propagating spikes whose contribution to LFPs is negligible (Mitzdorf 1985), such assumption seems to be reasonable inasmuch as synaptic afferents to target cells remain in place and the postsynaptic transmembrane currents elicited by them are for the most part circumscribed to the site where synapses make contacts at target dendrites (e.g., Herreras 1990; Leung et al. 1995). Besides, under experimental conditions with irregular LFP activity one can expect that the neuronal sources are largely independent in time. Accepting critically these theoretical observations we test here the applicability of ICA of LFPs recorded by multisite linear silicon electrodes that boost spatial resolution and eliminate problems inherent to distant recordings.

As a testbed we chose the monolayered CA1 region of the rat hippocampus that offers a number of advantages for verification of the applicability of the mixing model and the cellular identification of separated electrical sources. Most neurons in CA1 correspond to a single class of pyramidal cells oriented with their main axis in parallel, constituting a palisade of electric dipoles. The LFPs in this region are thus caused by synaptic activity in only one cell type. Conveniently, the different afferent neuron subpopulations as well as local interneurons have their axons terminating in discrete dendritic domains well known by histological studies (Lorente de Nó 1934; Somogyi and Klausberger

2005). Thus the ensemble activity of each afferent neuron subtype is expected to contribute to the LFP in spatially fixed bands corresponding to their synaptic territory onto pyramidal cell dendrites.

Before applying ICA to the spatial maps of LFPs recorded in the CA1 we employed algorithms to remove volume propagated activity from adjacent regions (cortex and CA3/dentate). Then we separated the dominant sources and assessed their specificity by correlation with local firing units. The identified dominant LFP sources were found similar among different experiments and animals. Their characteristic spatial distributions along the main CA1 axis were then used in a multicellular CA1 model to reconstruct LFP activity. The model results enabled direct comparison of contributing units to mixed LFPs and revealed complex phase-spike relations that reflect the spatial distribution and nature of synaptic inputs.

2 Methods

2.1 Experimental preparation

Female Sprague–Dawley rats (200–220 g) were anesthetized with urethane (1.2 g/kg i.p.) and fastened to a stereotaxic device. The body temperature was maintained at 37°C. The surgical and stereotaxic procedures were described elsewhere (Canals et al. 2005; Makarova et al. 2008). Concentric stimulating electrodes were positioned in the ipsilateral CA3 and in the perforant pathway for orthodromic activation of the CA1 pyramidal and dentate granule cell populations, respectively. Stimuli (0.07–0.1 ms square pulses, 0.1–0.5 mA) were applied to elicit the characteristic evoked potentials, which were used to guide the placement of recording probes [Fig. 1(a)]. Linear multisite probes (Neuronexus, A1x16-5 mm50–177 and A1x32-6 mm50–413) were lowered into the hippocampus (AP: 4.5–5.5, L: 2–3 mm from midline and bregma) and connected to a multiple high-impedance headstage. The signals were amplified and acquired using MultiChannel System recording hardware and software (50 kHz sampling rate). The recorded signals were downsampled to 1 kHz (referenced as LFPs) for ICA and to 25 kHz for sorting of unit activity. All experiments conformed to EC guidelines for animal care and the experimental protocols were approved by the Local Committee at the Cajal Institute.

2.2 Spike analysis

Spikes of individual neurons were isolated throughout the CA1 layers using wavelet enhanced principal component analysis method (Pavlov et al. 2007). To estimate the correlation of unit firings with the phase of LFP generators
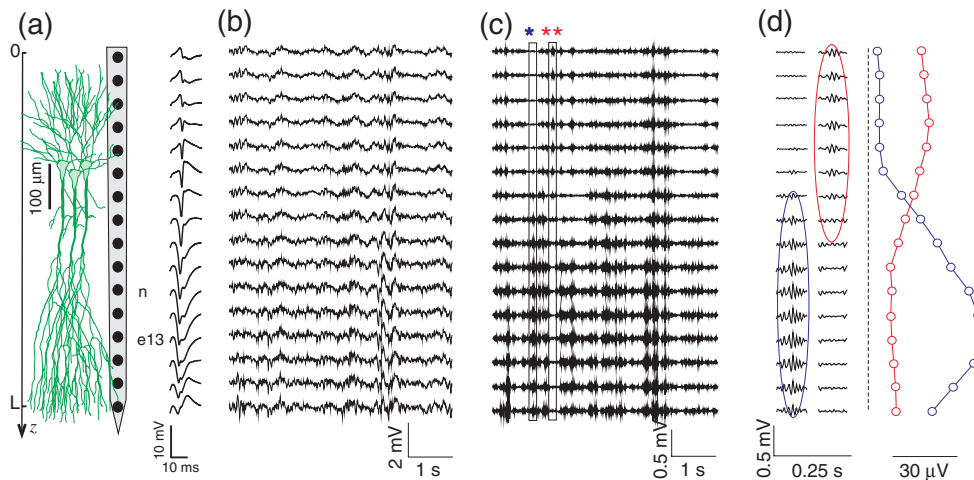
Fig. 1 Spatiotemporal diversity of LFP oscillations within the CA1 region. (**a**) Sketch of a linear probe completely covering the CA1 along the pyramidal neuron axis (*left*) and the guiding Schaffer-evoked potentials (*right*). (**b**) Raw LFP fragment during irregular activity. (**c**) Same LFP but filtered at the gamma band (30–100 Hz). Note multiple spatial distributions of epochs of gamma activity. (**d**) Two selected bouts of gamma activity covering the apical (*blue oval*) and the basal dendrites (*red oval*). Spatial profiles of the mean amplitude corresponding to the selected bouts are shown in the right

and raw LFPs we used the phase provided by the Hilbert transform and made a histogram of the phase values corresponding to spike occurrences. We used the Rayleigh test ($p<0.05$) for non-uniformity of circular data (Fisher 1996) to examine the significance of the unit to source couplings. The strength of the correlation was obtained by the mean resultant vector length over circular data ($0 \leq r \leq 1$). The correlation strength of units with LFP *vs.* units with isolated generators was compared by plotting the maximum value of r amongst all LFP channels (r_{LFP}) against the maximum r value over isolated generators (r_G). Significant deviations of the ratio r_{LFP}/r_G from 1 were used to find whether units are better correlated to isolated sources or to the raw LFP. The statistic *signtest* in MATLAB was used for population analysis.

2.3 General LFP model

In what follows we shall indistinguishably call sources of the LFP as generators. We can assume that during ongoing irregular activity in CA1 the generator activations, i.e., their dynamics in time, are mostly independent. Moreover, the current flow in extracellular space obeys quasistatic conditions (Nicholson and Freeman 1975). This together with the above mentioned stratified geometry enable a reasonably accurate modeling of the LFP along the main CA1 axis.

Under the assumption of spatial stationarity let

$$i_k(z,t) = I_k(z)s_k(t)$$

be the ensemble CSD of k-th generator driven by the corresponding interneurons or extrinsic fibers, where $I_k(z)$ and $s_k(t)$ are the spatial CSD loading over CA1 pyramidal

cells (z-axis) and time course of the generator activation, respectively. To approach the neurophysiologic terminology, the spatial *loadings*, $I_k(z)$, are also called here *spatial weights*. Then the LFP $u(z, t)$ is given by the Poisson's equation

$$\sigma \Delta u(z,t) = \sum i_k(z,t)$$

where we assume the constant conductivity $\sigma = 350 \ \Omega^{-1} \text{cm}^{-1}$ (López-Aguado et al. 2001). Thus the LFP can also be written as a sum of products of voltage loadings $V_k(z)$ and the generator activations $s_k(t)$

$$u(z,t) = \sum V_k(z)s_k(t), \ \ \Delta V_k(z) = I_k(z)/\sigma \quad (1)$$

Experimentally we sampled $u(z, t)$ along the main CA1 axis at 16 points $\{u_j(t)\}_{j=1}^{16}$, where t=0, 1, 2, ... is the discrete time. Then the spatial derivatives along the vertical z-axis can be approximated by the corresponding finite differences, and the LFP model reduces to:

$$u_j(t) = \sum V_{jk}s_k(t)$$

which is ready for ICA.

2.4 LFP preprocessing

Although ICA theoretically allows finding the unknown mixing matrix of the voltage loadings $V = \{V_{jk}\}$ directly from the spatially sampled potentials $\{u_j(t)\}$, such approach may not be optimal. Our experience and analysis of recordings made with 32-sites electrodes covering both CA1 and CA3 regions suggest that some strong extrinsic for CA1 generators can induce a notable electric potential within this region by volume conduction.

This may bias the ICA algorithm to detection of the strong but extrinsic generators, whereas weaker generators exclusively belonging to CA1 may be missed. Thus a preliminary data preprocessing suppressing the extrinsic generators may significantly improve the ICA performance in detecting intrinsic CA1 generators.

The boundary conditions and current conservation law yield

$$\sum_k i_k(0,t) = \sum_k i_k(L,t) = \int_0^L \sum_k i_k(z,t)\,dz = 0 \qquad (2)$$

where $L \approx 750$ μm is the length of pyramidal neurons. Equations (2) can be satisfied if, and only if, $V''_k(0) = V''_k(L) = 0$, and $V'_k(0) = V'_k(L)$. However, as mentioned above the volume propagation of the potential, e.g., from the adjacent CA3 region, can violate (2) within CA1. To eliminate the effect of the extrinsic sources and identify generators exclusively belonging to CA1, we first estimate activations of the extrinsic sources $a(t)$ and their loadings $U(z)$ (sFig. 1 in Supplemental materials). This can be done by finite difference approximation of the corresponding derivatives: $a_1(t) = u''_{zz}(0,t)$, $a_2(t) = u''_{zz}(L,t)$, and $a_3(t) = u'_z(0,t) - u'_z(L,t)$. Then the spatial loadings of the extrinsic sources are given by:

$$U(z) = C^{-1} \langle u(z,t), a(t) \rangle_t$$

where C is the covariance matrix of $a(t)$. Finally we obtain clean LFPs by subtracting the activity of extrinsic sources

$$\overline{u}(z,t) = u(z,t) - U(z)a(t) \qquad (3)$$

which then can be used for ICA.

2.5 ICA of LFPs

ICA assumes a statistical model in which the observed variables are a linear mixture of a priori unknown, mutually independent components that have non-Gaussian distributions. The above discussed LFP model (1) satisfies these assumptions. Thus we can apply ICA over previously cleaned LFPs (3), obtaining matrix of voltage loadings V and activations of the generators $s(t)$.

There are several ICA algorithms, which differ by estimation principles and objective functions. Two most popular are *fastica*, implementing the fast fixed-point algorithm (Gävert et al. 2005), and *runica*, implementing the infomax principle that is a part of EEGLAB (Delorme and Makeig 2004). The two algorithms are equivalent, at least in theory (for discussion see, e.g., Hyvarinen and Oja 2000). Our tests with experimental recordings also have shown that the spatial loadings and generator activations provided by both algorithms (in the case of *runica* extended-ICA option should be used) are similar (sFig. 2 in Supplemental materials). However, this similarity is restricted to the strongest generators only, and the algorithms may have different performance when dealing with weaker generators. In this paper we used the *runica* algorithm, which has widely been shown to be adequate for EEG applications.

One of the ICA ambiguities is the lack of proper ordering of the components. Unlike PCA there is no simple way to decide on which components are the most stable. Besides, real data sets may have different transient generators, whose "weights" in a long recording may be vanishing. ICA works best when given as large as possible amount of basically *similar* and mostly clean data. As a general rule, finding N stable generators requires $cN(N-1)/2$ data samples, where c is a multiplier and $N(N-1)/2$ is the number of weights to be estimated after data whitening. We noticed that the constraints (2) reduce the effective data dimension by three, i.e., for 16-channel data we have up to 78 weights. Then in 1 s time interval (about 4 theta cycles) we have about 13 pts/weight. Increasing further the time interval theoretically should facilitate ICA. However, using ICA for identification and suppression of artifacts (i.e., strong and stable generators) in EEG Castellanos and Makarov (2006) suggested the use of successive but relatively short time intervals.

To test the stability of LFP generators and identify the most stable we made use of ICA in two steps. First, we identify "global" generators by ICA of a sufficiently long recording (tens of seconds). Second, we divide the same recording into short-term contiguous epochs (each 1 s long) and apply ICA separately over these segments. We expect that stable strong LFP generators should be presented in all epochs and could be easily isolated by ICA in most of the time windows, whereas noisy, unstable, temporal, or weak generators will fluctuate and hence their spatial loadings will differ from epoch to epoch. Then by calculating similarity (see next subsection) between the "global" and "local" generators we can select those of them that are most stable over time. Indeed, this procedure showed that in a typical recording we can identify three to five stable LFP generators (sFig. 3 in Supplemental materials). Moreover, we found that stable generators always have smooth enough spatial voltage loadings $V_k(z)$, which is an important property, since the CSD loadings (1) can be computed as second order spatial derivatives of $V_k(z)$. The spatial profiles of $I_k(z)$ provide information on the localization of synaptic terminals causing the transmembrane active currents. Thus $I_k(z)$ cannot oscillate randomly but must be smooth enough functions, i.e., the emergent smoothness of $V_k(z)$ indirectly supports the choice of stable LFP generators.

2.6 Distance measure and templates for Independent Components

To define similarity between the spatial weight curves either obtained in different experiments or corresponding to different epochs, we introduce an appropriate distance measure. Once the distance between spatial loadings has been defined, we can cluster loading curves and decide on how many significantly different LFP generators can be identified from the data. Then the isolated clusters of loadings are used for obtaining (mean) templates of spatial weights and for estimating their variance.

To introduce the interloading distance we consider voltage loadings

$$V_k(x): \ \Omega \to R$$

as elements of a Hilbert space $H(\Omega)$, where $\Omega \subset R^3$ is an open set (e.g., CA1 region). It is noteworthy that due to the intrinsic ambiguity of ICA, $V_k(x)$ is defined up to a factor, i. e., if $V_k(x)$ is a loading then $\alpha V_k(z)$ ($\forall \alpha \in R$, $\alpha \neq 0$) is an equivalent loading. Indeed, any scalar multiplayer α in the loading $V_k(x)$ can always be canceled by dividing the corresponding activation by the same multiplayer: $s_k(t)/\alpha$. Such transformation does not alter the model (1), and consequently the generator loadings and activations can only be given in arbitrary units. This ambiguity is fortunately insignificant for our study, since we always can unequivocally calculate the potential and CSD induced by the k-th generator at a given electrode.

In the simplest case we equip $H(\Omega)$ with an inner product defined for an arbitrary pair of elements V_k and V_m as:

$$\langle V_k, V_m \rangle = \int V_k(x) V_m(x) dx, \ \forall V_k, V_m \in H(\Omega)$$

This definition captures the main properties of the voltage loadings and enables definition of the pair-wise inter-loading distance $d: \Omega \times \Omega \to [0, 1]$:

$$d(V_k, V_m) = 1 - \frac{|\langle V_k, V_m \rangle|}{\|V_k\| \|V_m\|} \quad (4)$$

where the norm is defined as usual $\|V_k\| = \sqrt{\langle V_k, V_k \rangle}$. The distance (4) is similar to the cosine metrics and it is bounded $0 \leq d \leq 1$. Moreover, $d=1$ for two orthogonal (completely different) loadings $V_k(x) \perp V_m(x)$, whereas $d=0$ for equivalent (identical) loadings $V_m(x) = \alpha V_k(x)$. Besides, the introduced distance measure is independent of the arbitrary scaling factors $\forall \alpha, \beta \in R$:

$$d(\alpha V_k, \beta V_m) = d(V_k, V_m)$$

Thus the distance measure (4) does not suffer from the ICA ambiguity.

Although the definition (4) is valid, it does not take into account the CSD origin of the LFPs and of the voltage loadings. For classification of the LFP generators (independent components) we should also consider their spatial derivatives. Thus we arrive to $H^2(\Omega) = W^{2,2}(\Omega)$ space with the inner product:

$$\langle V_k, V_m \rangle = \int_\Omega V_k V_m + \kappa \nabla V_k \nabla V_m + \kappa^2 \Delta V_k \Delta V_m \, dx, \quad (5)$$

$$\forall V_k, V_m \in H^2(\Omega)$$

where κ is a dimensional constant, which we set to $\kappa = 0.05$ mm^2. For V_k, $V_m \in H^2(\Omega)$ the distance definition (4) is maintained, but the inner product is taken in the H^2 sense. In the following we shall use the distance given by Eqs. (4) and (5).

2.7 Multicellular CA1 model of LFPs

The dorsal CA1 region was simulated as an aggregate of pyramidal model units preserving an experimentally observed cell density of 64 neurons oriented in parallel in a 50×50 μm antero-lateral lattice (Boss et al. 1987) forming a cylinder of 0.5 mm in diameter (877 units, Fig. 5(a)). This aggregate size ensures near maximum contribution of extracellular synaptic currents by volume conduction to a recording track in the center of the cylinder aggregate in parallel to the somatodendritic axis (Varona et al. 2000). Dorso-ventral extension was set to 0.75 mm (from the alveus to the distal apical tuft). Units were spatially distributed so that their somata form a 50 μm thick stratum with 4 layers of even density. The LFP was calculated at each of 16 "recording" points 50 μm apart simulating a vertical track

$$\Phi(t) = \frac{1}{4\pi\sigma} \sum_{i=1}^{\text{cells}} \sum_{j=1}^{\text{comps}} \frac{I_{m_{ij}}(t)}{r_{ij}} \quad (6)$$

where $I_{m_{ij}}$ is the total transmembrane current at the j-th compartment of neuron i, and r_{ij} is the distance from the recording point to that compartment. Thus, compartments are treated as point current sources in a conducting homogeneous medium ($\sigma = 350$ [Ωcm]$^{-1}$).

A simplified single-neuron model was built using 75 lumped equivalent cylinders 10 μm long representing the apical and basal dendritic portions (50 and 25 compartments, respectively) and an interposed spherical soma. Standard electrotonic parameters were employed (Varona et al. 2000) with some modifications. In order to approach realistic values of the total membrane capacitance, the diameter of cylinders was variably increased (unit surface was 22828 μm^2). Since this introduced an undesirable variable axial resistance that influences strongly the spread

of internal currents (hence transmembrane current distribution), we introduced a variable factor to modify axial resistance between consecutive compartments. The input resistance measured at the soma was 66 MΩ, and τ was 23 ms, values closed to those reported for whole cell recordings (e.g., Spruston and Johnston 1992). In this simplified model we have not implemented active (V-dependent) channels to facilitate the observation of interactions between different synaptic inputs.

Up to three synaptic inputs were implemented using the spatial distributions of the current sources recovered by the second spatial derivative of the dominant generators obtained in the experimental analysis. For example, a sandwich-like spatial distribution of a CSD loading $I_k(z)$, e.g., positive in the middle and negative on sides, suggests an active current source in the middle enclosed between passive return currents. Then we expect inhibitory synaptic terminals localized at this location (sFig. 4 in Supplemental materials). Spatially extended synaptic inputs can lead to central cancelation effect (Makarova et al. 2009), i.e., there appears an effective depression in the middle of the spatial distribution of $I_k(z)$. The location and spatial distribution served to associate each of these generators to known excitatory and inhibitory synaptic inputs according to distributions of axonal terminal fields of extrinsic cells and local interneurons (Lorente de Nó 1934, Buzsaki 1984). Excitatory synaptic input of the non-NMDA type was simulated as a dual exponential function conductance with a reversal potential of 0 mV, τ1=10.8 ms, and τ2= 2.7 ms (for details see Ibarz et al. 2006). Inhibitory synaptic conductances of the GABA$_A$ and GABA$_B$ types followed an alpha function with τ of 7 ms and 35 ms, and reversal potential of −75 mV and −90 mV, respectively.

Synaptic bombardment was simulated by random inputs of presynaptic spikes for each generator. Phase-spike correlations of model LFPs can thus be constructed that enables global qualitative comparison with real LFPs and exploration of factors contributing to layer dependent variations in phase-spike correlations.

3 Results

3.1 Spatiotemporal diversity of LFP

Besides the well-known theta rhythm, irregular activity is the principal manifestation of raw LFPs in the hippocampus [Fig. 1(b)]. Its composite nature can be easily appreciated in filtered LFP fragments. Figure 1(c) illustrates LFPs filtered in the gamma band (30–100 Hz). Although the strongest activity in this frequency range was observed in the CA3/dentate region (Bragin et al. 1995), the CA1 also shows an extraordinary diversity of gamma bouts extending through

different groups of electrodes. In a top-to-bottom inspection by the naked eye, dozens of spatiotemporal configurations can be appreciated with a highly variable overlap. Some gamma epochs involve all electrodes and display increasing, decreasing or near constant amplitude in space. The others have a certain number of gamma waves in a set of electrodes that merge with longer or shorter epochs in the adjacent electrodes. A closer look would augment the diversity by discovering phase variations of the gamma cycles along the CA1 z-axis. Figure 1(d) shows two selected bouts of gamma activity and the corresponding spatial distributions of their mean amplitudes obtained by averaging over the epoch time window. The epochs exhibit transient activity involving distinct spatial domains along the z-axis of CA1 pyramidal cell. Similar displays of LFPs filtered within other frequency bands also present more or less evident heterogeneous spatiotemporal configurations of activity. This suggests the presence of multiple subcellular generators of LFPs with a significant spatiotemporal overlapping in the same neuron conductor. To isolate the converging sources of activity in the next section we shall apply ICA to the spatial maps of the LFPs covering the CA1 dorsoventral axis.

3.2 Isolation of mixed LFP generators

First, we eliminated volume propagated contributions from nearby regions (cortex and CA3/dentate) as described in Methods. Thus we ensure that generators obtained from the analysis of LFPs recorded within the CA1 are indeed produced within this subfield. In order to test ICA stability we employed two different time strategies combining long and short LFP epochs (see Section 2 and sFig. 3 in Supplemental meterials), and compared results among different animals. Figure 2 shows the voltage loadings $V_{1,2,3}(z)$ (spatial weight curves) of three most powerful LFP generators G1–G3 (explained variance 81%) found in one recording lasting 100 s (an epoch with irregular activity has been selected). The decomposition of a typical LFP fragment into activity of these three generators, $s_{1,2,3}(t)$, is shown at the bottom of Fig. 2. Inspection of the mean absolute residual $w(t)$ validates the separation. In the soma region (electrode 6) the voltage loadings corresponding to generators G2 and G3 invert their polarity, while G1 is the main contributor. As expected, the epochs overlap in time and space in a complicated manner, though ICA identified three main independent LFP generators. These three generators were stable over time, and their spatial distributions were maintained in different epochs recorded within several hours in the same animal, and regardless of whether theta or irregular activity was the dominant LFP pattern. Other stable generators that contribute a small variance to LFPs can also be obtained; however, their analysis requires
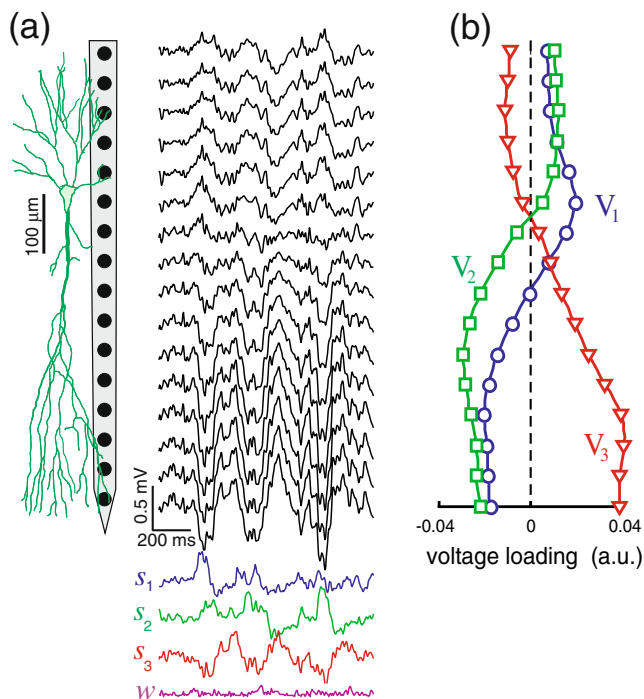
Fig. 2 Decomposition of LFPs into three underlying independent generators G1–G3 by ICA. (**a**) Schematic representation of recording points and a fragment of raw LFPs (*black traces*). Three main generators have been isolated from raw LFPs. (**b**) Spatial distribution of the voltage loadings $V_{1, 2, 3}(z)$ corresponding to the isolated generators G1–G3, whose activations $s_{1, 2, 3}(t)$ [shown time interval corresponds to the LFP fragment in (**a**)] are shown at the bottom. $w(t)$ is the mean absolute residual

transmembrane currents (current sinks and sources) specific for each input. This can be assessed by CSD analysis that eliminates volume propagation in the CA1 area and provides the spatial distribution of current density along the dendritic field of pyramidal cells. We adopted the conventional unidimensional approach (Nicholson and Freeman 1975; Herreras 1990) used for raw LFPs. The CSD of the isolated generators can be obtained by the second spatial derivative of the respective curves of voltage loadings (1). The CSD spatial profiles for G1–G3 averaged over five animals are shown in Fig. 3(b). Inspection of the CSD profiles provides information (see below) on the distribution of synaptic inputs for the generators. To gain temporal dynamics, i.e. the population activity induced by synaptic inputs, one can multiply the obtained spatial distribution by the corresponding activation $s_k(t)$ also provided by ICA.

3.3 Relation of isolated generators to unit activity

The time evolution of the activations $s_k(t)$ of the isolated generators can be used to study functional couplings and other dynamical aspects, such as, e.g., state-dependent modulation. Particularly, quantification of the activity of the LFP generators enables the study of temporal correlations with the simultaneously recorded unit activity. Neuronal spikes were obtained throughout the CA1 layers by high-pass filtering the same recordings and subsequent sorting using the wavelet enhanced PCA algorithm (Pavlov et al. 2007). In the CA1 field, all cells recorded outside the

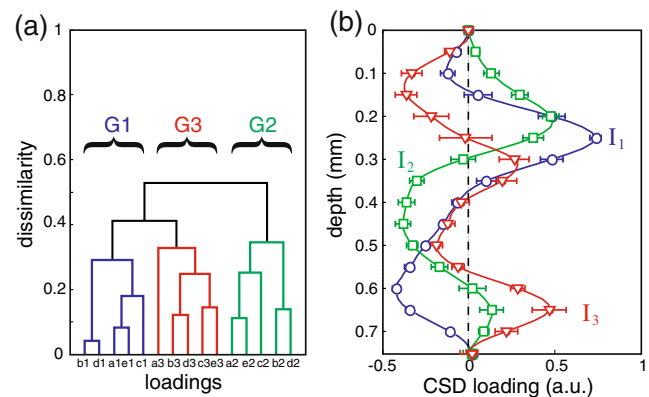prior treatment of signals and fine tuning of the ICA algorithm.

To confirm the universality of the found dominant generators we repeated the above described procedure using LFPs recorded in five animals. Visual inspection of the obtained voltage loadings revealed an important feature: the presence of a stable set of the LFP generators in any examined location of the dorsal CA1 region with highly repeatable shapes of the spatial distribution curves across different animals. To quantify inter-experimental similarity we introduced an appropriate distance measure between generator loadings (see Section 2), and evaluated pair-wise dissimilarity between spatial loadings of all major generators found in five experiments. Figure 3(a) shows hierarchical clustering with the average-linkage algorithm (maximizing the cophenetic correlation coefficient). The three generators G1–G3 are found in all five experiments, thus confirming universality of the LFP generation mechanisms in CA1. Some dispersion in the shape of loading curves was grouped by the cluster analysis. This most likely reflects the variable mutual interference of concurrent inputs.

The stable shape of the spatial distribution curves ensures their origin in fixed domains of inward and outward

Fig. 3 Stability of the main CA1 generators across animals. (**a**) Dissimilarity index (interloading distance) was employed to group the curves of spatial weights found in five animals (*letters a–e* mark the animals and numbers 1–3 correspond to the loadings). *Curve clustering* indicates three different generator groups with significantly different spatial distributions of loadings. (**b**) The second spatial derivative of the voltage loadings was obtained to derive the transmembrane current density distribution corresponding to each generator ($I_{1, 2, 3}(z)$), and averaged across five animals (confidence intervals show standard error). The vertical axis covers the somato-dendritic extension of CA1 pyramidal cells

pyramidal layer are considered putative interneurons (Ranck 1973; Herreras et al. 1988). Figure 4(a) illustrates 30 s segment of spontaneous irregular LFP at electrode 13, the digitalized firing events of a putative interneuron simultaneously recorded in the stratum radiatum [cell n in Fig. 1(a)], and the time varying activations of the generators G1–G3 contributing to the whole LFP.

Stable sources of LFP activity disentangled by ICA must keep fixed spatial domains, as derived from its mathematical essence, which in the CA1 region should correspond to specific portions (along z-axis) of the dendritic tree of a pyramidal neuron activated by different subtypes of local interneurons and extrinsic cells. If that is so, and the used technique indeed separates LFPs into activities provoked by different neural subpopulations, one may predict that the correlation of firing of local cells with some of the isolated generators should be significantly stronger than with raw LFP signals that are jointly contributed by all of them. We test this prediction by comparing the correlation index r for putative interneurons with LFP signals *vs.* activations of isolated generators.
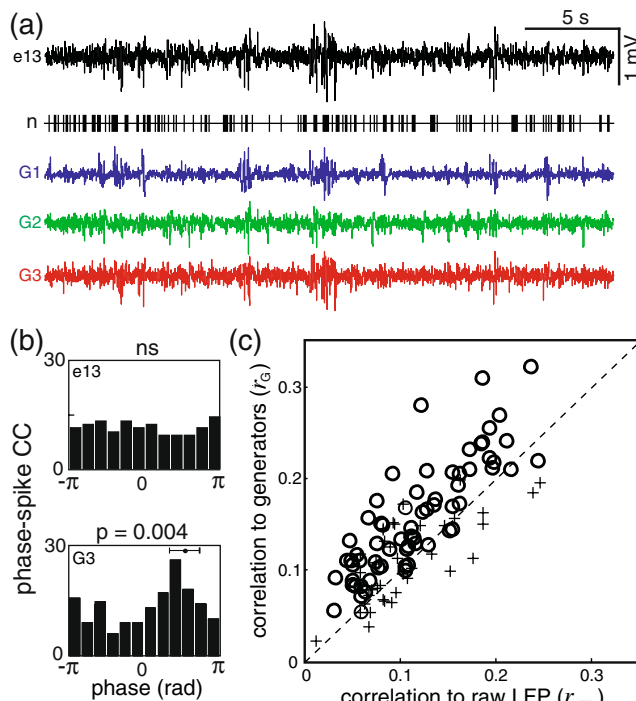
Fig. 4 Quantitative readout of isolated LFP generators and their relation with firing units. (**a**) Raw LFP recorded in the apical dendrites (e13), spike train of a selected unit n (see positions in Fig. 1(a)), and time courses of activity of isolated generators G1–G3 (arbitrary proportional units). (**b**) Phase-spike correlation histograms for the sample unit to raw LFP (e13) and to isolated generator G3 (calibration: radians and counts). (**c**) Generators-spike trains *vs.* raw LFP-spike trains correlations for local putative interneurons recorded simultaneously with LFP. For raw LFP the highest (among 16 channels) correlation coefficient was used

Figure 4(b) shows a representative example of the cross-correlation histograms of firing events of the putative interneuron n [Fig. 1(a)] with the phase of raw LFP (electrode 13) and with the phase of G3. The neuron has no statistically significant phase correlation with the raw LFP, but selective strong correlation ($r=0.18$, $\varphi \approx \pi/2$) with G3 (Raleigh test, $p=0.004$). This suggests that the neuron belongs to the population causing the activity of G3. We found 70 out of 126 units significantly correlated with at least one generator [Fig. 4(c), circles], whilst 39 showed no correlation [Fig. 4(c), crosses]. A total of 17 units had too low firing rate and could not be used for the study. Most correlated units fell above the midline (signtest, $p=10^{-7}$), indicating stronger correlation with at least one isolated generator than to any raw LFP channel. Correspondingly, non-correlated units fell around the midline (signtest, $p=10^{-5}$), hence they show no preference to LFPs nor to generators, as also expected. Thus the use of ICA-isolated generators provides direct matching of particular LFP events to their neuronal sources, and indeed overcomes uncertainty of the LFP mixture. We estimate that about 65% of putative interneurons in CA1 belong to populations related to the most powerful LFP generators G1–G3.

3.4 Simulated LFP and exploration of phase-spike correlations

Knowing the spatial distribution of the population transmembrane currents for the three main generators allowed the simulation of CA1-like LFPs in an aggregate model of the CA1 [Fig. 5(a), see Section 2]. The spatial weights of the inhibitory (G1 and G3) and excitatory (G2) inputs are depicted in Fig. 5(a). Note that the spatial distributions of synaptic weights differ from the spatial distributions of the isolated generators [Fig. 3(b)], as the former are restricted to the domain of active currents, while the latter also include passive currents (see also sFig. 4 in Supplemental materials). In the example illustrated in Fig. 5 we employed random synaptic bombardment for all three generators with average frequencies of 10 Hz for G1 and G3, and 50 Hz for G2. This combination was chosen to obtain an average excitatory and inhibitory baseline conductance of 30 and 70 nS, respectively, which are within experimental ranges found in cortical cells (Rudolph et al. 2005). Figure 5(b) shows an example of simulated LFP traces of about 500 µV (peak to peak) amplitude. Oscillations in a wide frequency band can be appreciated in the simulated segment, which closely resemble irregular LFPs observed experimentally [Figs. 1(b) and 2(a)].

Once the simulated LFPs have been obtained we can study the spike-phase correlations that reflect the temporal relation between presynaptic spikes and the postsynaptic currents producing the LFPs, regardless of the time
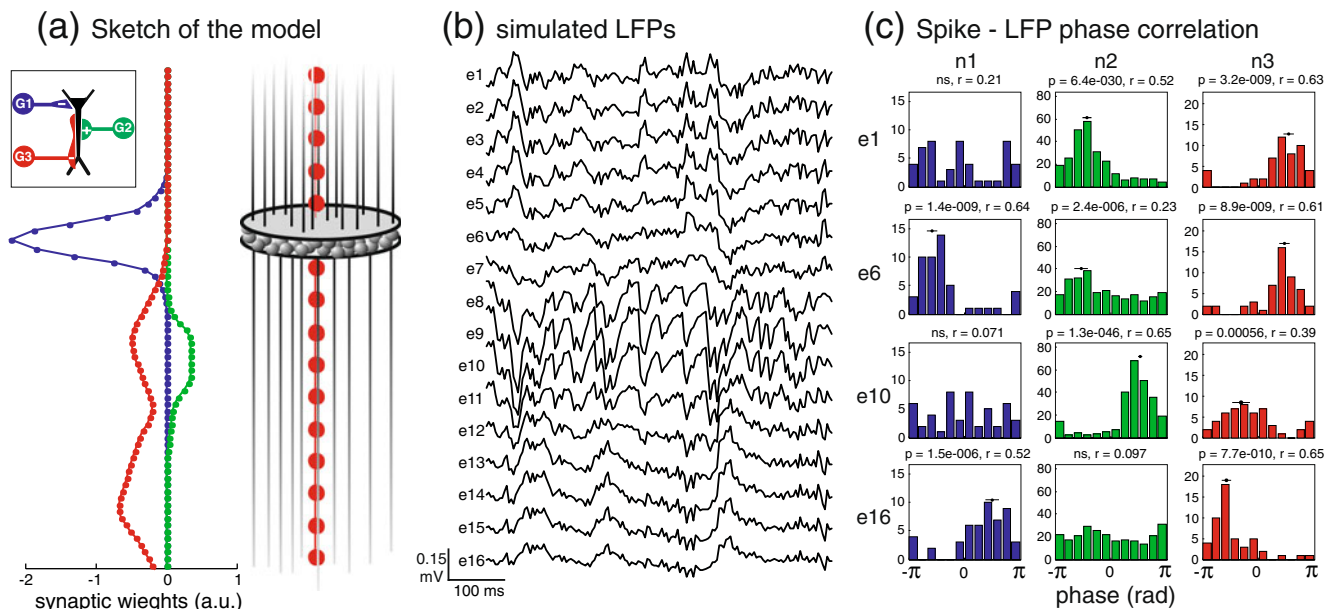
Fig. 5 Simulation of LFPs. (**a**) A multicellular model of simplified pyramidal cells was built to simulate LFPs along a vertical track of 16 recording points in the center of a cylinder of tissue (500 μm diameter) made up of a monolayer of pyramidal cells (*right*) ordered as in the CA1. The spatial distributions of three employed synaptic inputs (two inhibitory and one excitatory) are shown in the *left*. The polarity of the synaptic weight indicates inhibitory (−) and excitatory inputs (+). The *inset sketch* shows the local circuit included in the model. (**b**) A segment of LFPs calculated for the recording track using a random spike train for each of the three synaptic distributions. Multiple oscillations and changing polarities can be appreciated, with the highest variance concentrated in the stratum radiatum (electrodes 8–12). Simulated LFPs in CA1 do not include the volume propagated potentials from adjacent CA3/dentate regions. (**c**) Phase-spike correlations of each presynaptic spike train to its associated LFP. The preferred phase and statistical significance of correlation varied with the position of recording according to the spatial distribution of the synaptic input (see main text for explanation)

structure of the inputs. Figure 5(c) shows these correlations of LFPs and the presynaptic spikes at different locations along the z-axis of the pyramidal cell. As expected, the correlation strength varies in a layer-specific manner. Indeed, each spike train shows significant correlations with LFPs, but only at specific recording locations. For instance, G1 (blue histograms) has strong correlation with e6 (location corresponding to active currents) and e16 (location corresponding to passive currents), where LFPs caused by this neuron are large [whether positive or negative; see Figs. 2(b) and 3(b)], but not at the distant site (e1), nor at the loci of phase reversal (e10) where the generator strength is small.

Since stratified synaptic currents produce both positive and negative LFPs in different domains of the postsynaptic cell according to the distribution of active and passive (return) transmembrane currents, we may expect this to be reflected in the phase-spike histogram. Indeed, inhibitory inputs (G1 and G3) showed a preferred negative phase correlation with LFPs recorded in loci of active domains (e.g., e6 in the soma layer for G1 and e10–e16 in the apical dendrites for G3) and a positive phase in domains were passive currents return to the extracellular space (e16 in the distal apical dendrites for G1 and e1–e6 in somato-basal domains for G3). The opposite occurs for excitatory inputs

(G2) that produce LFPs of opposite polarity with respect to the active input site.

As it was made above for experimental data, we assessed the specificity of the information contained in model LFPs produced by one generator (i.e., a single generator is active while the others are suppressed) versus the mixed (raw) model LFPs by comparing the mean (throughout all layers) phase-spike correlation in the two cases (Fig. 6). We found a significantly higher correlation in all three spike trains when correlated to LFPs caused by their own generators only (open bars) as compared to the mixed LFPs (filled bars). Some general conclusions can be drawn from the inspection of phase-spike correlations throughout layers. The mean correlation of a given spike train with raw LFPs is not necessarily related to its relative contribution (variance) to the LFPs, but to the spatial extension of the synaptic input along the postsynaptic cell (e.g., compare correlations for the strongest generator G1 *vs.* the weakest G3, filled bars in Fig. 6). The opposite happens for correlation of spike trains with their own LFP generators, i.e., the wider is the distribution of the synaptic input the smaller is the correlation (e.g., G1 *vs.* G3, open bars in Fig. 6). These observations highlight the importance of the intensity and spatial distribution of active synaptic currents contributing to LFP generation.
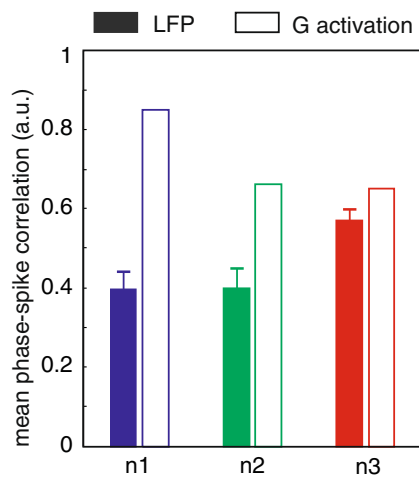
Fig. 6 Phase-spike correlation for simulated complete LFPs vs. LFPs contributed by single presynaptic inputs (i.e., generators). Individual spike trains always presented lower mean correlation with the mixed LFP (*filled bars*, confidence intervals show standard error over 16 channels) than to their own activation (*open bars*, S.E. is negligible). The magnitude of the mean correlation varied with the spatial features of each synaptic input and their mixture (see main text for explanation)

4 Discussion

Multiple neuron subpopulations contribute to the generation of classic LFP oscillations recorded from a single electrode. We have shown that their ensemble afferent activity can be separated, and correlated to the firing of specific local non-principal cells using ICA and data clustering. Isolated generators indeed hold more specific information than raw LFPs. Model LFP reconstruction using this approach enables the use of phase-spike correlations for linking the global presynaptic activity of a specific neuron subpopulation to the spatiotemporal properties of the generated postsynaptic currents that give rise to LFPs. Besides, simulated LFPs obtained from a realistic model resembling the architectonic and electrophysiological properties of CA1 can be used to test and validate different signal processing methods.

4.1 Advantages of ICA for source localization

The use of ICA for blind isolation of sources in mixed signals has been well established in different fields, including fMRI, surface EEG of the human scalp (e.g., Jung et al. 2005) and also in deep LFP recordings (Tanskanen et al. 2005), but to our knowledge this is the first successful attempt to disentangle deep brain recordings into the separated activity of the different contributing generators. Although other methods provide valuable information, only ICA has the capability to resolve the contributing independent sources offering precise spatio-

temporal information (Mouraux and Iannetti 2008). For instance, Fourier analysis often employed for separation and quantification of activity in different frequency bands cannot unmix contributions from two different afferent presynaptic populations with overlapping terminal fields. Moreover, specific frequency bands in the LFP do not define the activity of particular neuron classes nor elemental synaptic events. Besides, while most population studies focus on rhythmic or oscillatory LFP events, which simplifies correlation with certain behaviors, the prevailing macroscopic activity reflecting network operation and information processing is irregular. ICA makes no assumption on the frequency content of the signals and performs properly with complex nonperiodic LFP events. Thus one of the major advantages of the approach discussed here is its applicability to irregular LFP signals recorded with or without sensory stimulations. The validity of ICA is given by the stationary (in space) nature of the synaptic currents, thus the number and shape of spatial distributions of found generators are the same during irregular or rhythmic oscillations in raw LFPs, as can be expected from the varying temporal dynamics of local and extrinsic firing units producing the synaptic currents. The simplified model we used here to simulate numerically LFPs illustrates this point and highlights the possibilities of ICA to study quantitatively the global activity of multiple neuron subpopulations.

4.2 The nature of isolated generators

The electrical sources found by ICA are immobile on the experimental time and space scales (e.g., spikes slowly propagating over long distances should be treated differently). The only cytoarchitectonic element that can produce LFP activity with stable spatial domains in this stratified cerebral region is the axonal terminal fields of particular afferent neural populations. The problem of interpreting the nature of the separated generators is simplified by the use of linear probes in the monolayered CA1 that yield subcellular precision of the spatial distribution of sources. Such simplification does not work in the neocortex where the dendrites of pyramidal cells belonging to different layers share spatial domains. Nevertheless, our methodology can be applied to cortical recordings, although some adjustments of the algorithm taking into account the multilayered specificity of the cortical structures should be implemented.

Pyramidal cells constitute the largest neuron population in the CA1 field (~95%). Their parallel arrangement and bipolar anatomy produce open fields; hence they provide most of the postsynaptic current rising LFPs in this region. Local interneurons are few and mostly multipolar (Somogyi and Klausberger 2005), hence their synaptic activation produces closed fields and hence contributes negligibly to

the LFP. However, their local axons contact with pyramidal cells in discrete somatodendritic bands and constitute a major component of the net synaptic current (e.g., Rudolph et al. 2005). We thus propose that the three isolated generators G1–G3 correspond to population readout of the synaptic input from functional classes of local interneurons or extrinsic projection cells with partially overlapped synaptic territories onto pyramidal cells.

A large proportion of local putative interneurons show stronger correlation with some of the isolated generators than with raw LFPs. Indeed, the firing rate of many CA1 interneuron classes (but not all) is very high as compared to the almost silent behavior of pyramidal cells (Ranck 1973; Herreras et al. 1987), which is consistent with the powerful inhibitory control in this region (Buzsaki 1984). The emerging view is that each generator is causally related to the activity of specific groups of interneurons. We estimate that about 65% of interneurons in CA1 belong to populations involved in the activity of G1–G3. Whether these units are pre or postsynaptic or both requires detailed analysis of spike-phase correlations. The spatial distribution of the underlying currents is an important feature that can be matched to axonal terminal fields of known afferent subpopulations. Based on this information and correlation analysis with firing units located in different strata we identified G1 and G3 with inhibitory currents from perisomatic and apical targeting local interneurons, while G2 is consistent with the spatial distribution of currents generated at the termination zone of the Schaffer/commissural inputs and hence may be fitted by excitatory input from CA3 pyramidal cells or inhibitory inputs from Schaffer collateral-associated interneurons (Somogyi and Klausberger 2005). Additional work is required to explain the adscription of the considerable fraction (about 35%) of uncorrelated local units. One possibility is that the lack of specific correlation to either raw LFP or some of the isolated generators is explained by the fact that they belong to a neuron class involved in multiple local circuits or operating at very long timescales. Alternatively, their axonal field is small and/or their firing rate too low to contribute notably to the net variance of LFP, remaining then below statistical significant contribution. Indeed, we found additional generators contributing a small variance after filtering the raw signals within narrow bands and playing with short time windows, which rises chances of transient generators to be detected by ICA.

A confounding factor in LFP-unitary combined studies is that hippocampal interneurons respond to practically any extrinsic input as well as to firing of pyramidal cells (Ranck 1973; Buzsaki 1984), hence correlated firings are expected even when each local neuron subtype takes part in different local circuits and produces synaptic currents in different parts of the pyramidal somatodendritic axis (Somogyi and

Klausberger 2005). However, the model study already proved notable utility of ICA in this respect. The laminar analysis of phase-spike correlations revealed a spatial distribution of preferred phase, polarity and dispersion in agreement with the distribution of the active synaptic currents underlying each LFP generator. Certainly, the model LFPs were produced by the activity of single spike trains taking the role of entire afferent subpopulations. Therefore, at this stage we cannot ascertain whether such degree of accuracy can be obtained in phase-spike correlations for individual neurons. In any case, the combination of ICA of LFPs and laminar analysis of spike-phase correlation of local (and extrinsic) units reveals as a powerful tool to discriminate unit contribution to specific LFP events even when different unit subtypes fire in correlation.

4.3 Simulated LFPs

The present numerical simulation of LFPs follows the standard design of our former aggregate models (Varona et al. 2000; Ibarz et al. 2006) with some modifications. Here we fed the model with important experimental information: the spatial distribution of currents for the three generators that produce the bulk of the LFP variance. Oscillations of different frequency can be appreciated in the simulated segment that closely resemble real LFPs. Stronger realism requires the model upgrading in several aspects, such as the use of branched neurons and the inclusion of active membrane channels. In particular, the large surface of dendritic trees and axial resistance are important factors defining the spatial distribution of evoked field potentials (Varona et al. 2000; Pettersen and Einevoll 2008). In the present model we sought to simplify the interpretation of isolated generators by avoiding confounding elements, but introduced a set of factors to minimize error arisen from the inaccuracy of the morphoelectrotonic structure of the simplified model units.

Though being simplified the model captures many realistic mechanisms involved into generation of LFPs such as spatial extension, current mixing, mutual cancelation or amplification of synaptic currents provoked by different inputs, etc. Thus the model is far more complex than the majority of the mathematical models used in the literature to validate performance of signal analysis methods including ICA. This makes it a good testbed for checking, testing, comparing, and analyzing different algorithms for LFP analysis.

A more defying problem is the contribution of intrinsic currents to LFPs (e.g., Murakami et al. 2003; Glasgow and Chapman 2008). If such contribution were strong enough to initiate active propagation of currents within dendrites, the assumption of stationary currents required for ICA application would be challenged and we would have to admit a

certain error in the curves of spatial weights obtained for isolated LFP generators. Preliminary results obtained with morphologically realistic units including active membrane currents indicate however that this factor does not introduce a noticeable error in the localization of the synaptic bands for each generator. Most likely, slow dendritic currents, which cannot be separated from the synaptic ones, are integral part of each isolated generator. In parallel studies (Makarova et al. 2008) we found that a major factor defining the amplitude and spatial distribution of aggregate postsynaptic currents is central spatial cancellation within postsynaptic membranes of individual membranes. For widely distributed currents this phenomenon becomes especially significant even overcoming the influence of the above mentioned electrotonic parameters (Makarova et al. 2010), such as those produced by axonal fields of inhibitory interneurons in the stratum radiatum (Somogyi and Klausberger 2005). Such effect may explain the bimodal (depressed at the middle) spatial distribution of generator G3 found here.

In short, the methodology for separation of mixed sources in the EEG/LFP presented here opens new avenues to disclose the functional neural circuitry from ordinary LFP recordings and inferring on its dynamic properties.

References

Bédard, C., Kröger, H., & Destexhe, A. (2004). Modeling extracellular field potentials and the frequency-filtering properties of extracellular space. *Biophysical Journal, 86*(3), 1829–1842.

Bell, A., & Sejnowski, T. (1995). An information-maximization approach to blind separation and blind deconvolution. *Neural Computation, 7*, 1129–1159.

Boss, B. D., Turlejski, K., Stanfield, B. B., & Cowan, W. M. (1987). On the numbers of neurons in fields CA1 and CA3 of the hippocampus of Sprague–Dawley and Wistar rats. *Brain Research, 406*, 280–287.

Bragin, A., Jandó, G., Nádasdy, Z., Hetke, J., Wise, K., & Buzsáki, G. G. (1995). Gamma (40–100 Hz) oscillation in the hippocampus of the behaving rat. *Journal of Neuroscience, 15*(1), 47–60.

Buzsaki, G. G. (1984). Feed forward inhibition in the hippocampal formation. *Progress in Neurobiology, 22*, 131–153.

Canals, S., López-Aguado, L., & Herreras, O. (2005). Synaptically-recruited apical currents are required to initiate axonal and apical spikes in hippocampal pyramidal cells: modulation by inhibition. *Journal of Neurophysiology, 93*, 909–918.

Castellanos, N. P., & Makarov, V. A. (2006). Recovering EEG brain signals: Artifact suppression with wavelet enhanced independent component analysis. *Journal of Neuroscience Methods, 158*, 300–312.

Choi, S., Cichocki, A., Park, H. M., & Lee, S. Y. (2005). Blind source separation and independent component analysis: a review. *Neural Information Processing - Letters and Reviews, 6*, 1–57.

Delorme, A., & Makeig, S. (2004). EEGLAB: an open source toolbox for analysis of single trial EEG dynamics including independent component analysis. *Journal of Neuroscience Methods, 134*, 9–21.

Einevoll, G. T., Pettersen, K. H., Devor, A., Ulbert, I., Halgren, E., & Dale, A. M. (2007). Laminar population analysis: estimating firing rates and evoked synaptic activity from multielectrode recordings in rat barrel cortex. *Journal of Neurophysiology, 97*(3), 2174–2190.

Fisher, N. I. (1996). *Statistical analysis of circular data*. Cambridge University Press.

Gävert, H., Hurri, J., Särelä, J., & Hyvärinen A. (2005). Matlab implementation of fastica is available at http://www.cis.hut.fi/projects/ica/fastica/.

Glasgow, S. D., & Chapman, C. A. (2008). Conductances mediating intrinsic theta-frequency membrane potential oscillations in layer II parasubicular neurons. *Journal of Neurophysiology, 100*(5), 2746–2756.

Herreras, O. (1990). Propagating dendritic action potential mediates synaptic transmission in CA1 pyramidal cells in situ. *Journal of Neurophysiology, 64*, 1429–1441.

Herreras, O., Solís, J. M., Martín del Río, R., & Lerma, J. (1987). Characteristics of CA1 activation through the hippocampal trisynaptic pathway in the unanaesthetized rat. *Brain Research, 413*, 75–86.

Herreras, O., Solís, J. M., Muñoz, M. D., Martín del Río, R., & Lerma, J. (1988). Sensory modulation of hippocampal transmission. I. Opposite effects on CA1 and dentate gyrus synapsis. *Brain Research, 451*, 290–302.

Hyvärinen, A., & Oja, E. (2000). Independent component analysis: algorithms and applications. *Neural Networks, 13*(4–5), 411–430.

Ibarz, J. M., Makarova, I., & Herreras, O. (2006). Relation of apical dendritic spikes to output decision in CA1 pyramidal cells during synchronous activation: a computational study. *European Journal of Neuroscience, 23*, 1219–1233.

Jung, K. Y., Kim, J. M., Kim, D. W., & Chung, C. S. (2005). Independent component analysis of generalized spike-and-wave discharges: primary versus secondary bilateral synchrony. *Clinical Neurophysiology, 116*, 913–919.

Kocsis, B., Bragin, A., & Buzsáki, G. G. (1999). Interdependence of multiple theta generators in the hippocampus: a partial coherence analysis. *Journal of Neuroscience, 19*(14), 6200–6212.

Leung, L. S., Roth, L., & Canning, K. J. (1995). Entorhinal inputs to hippocampal CA1 and dentate gyrus in the rat: a current-source-density study. *Journal of Neurophysiology, 73*(6), 2392–2403.

López-Aguado, L., Ibarz, J. M., & Herreras, O. (2001). Activity-dependent changes of tissue resistivity in the CA1 region *in vivo* are layer-specific: modulation of evoked potentials. *Neuroscience, 108*(2), 249–262.

Lorente de Nó, R. (1934). Studies of the structure of the cerebral cortex. II. Continuation of the study of the ammonic system. *Journal of Psychology and Neurology, 46*, 113–177.

Makarova, I., Gómez-Galán, M., & Herreras, O. (2008). Layer specific changes in tissue resistivity and spatial cancellation of transmembrane currents shape the voltage signal during spreading depression in the CA1 in vivo. *European Journal of Neuroscience, 27*, 444–456.

Makarova, J., Makarov, V. A., & Herreras, O. (2010). A model of sustained field potentials based on polarization gradients within single neurons. (to appear in the Journal of Neurophysiology).

Makeig, S., Debener, S., Onton, J., & Delorme, A. (2004). Mining event-related brain dynamics. *Trends in Cognitive Science, 8*, 204–210.

Mitzdorf, U. (1985). Current source-density method and application in cat cerebral cortex: investigation of evoked potentials and EEG phenomena. *Physiological Reviews, 65*, 37–100.

Montgomery, S. M., Betancur, M. I., & Buzsáki, G. G. (2009). Behavior-dependent coordination of multiple theta dipoles in the hippocampus. *Journal of Neuroscience, 29*, 1381–1394.

Mouraux, A., & Iannetti, G. D. (2008). Across-trial averaging of event-related EEG responses and beyond. *Magnetic Resonance Imaging, 26*(7), 1041–1054.

Murakami, S., Hirose, A., & Okada, Y. C. (2003). Contribution of ionic currents to magnetoencephalography (MEG) and electro-encephalography (EEG) signals generated by guinea-pig CA3 slices. *Journal of Physiology, 553*(3), 975–985.

Nicholson, C., & Freeman, J. A. (1975). Theory of current source-density analysis and determination of conductivity tensor for anuran cerebellum. *Journal of Neurophysiology, 38*(2), 356–368.

Nunez, P. L., & Srinivasan, R. (2006). *Electric fields of the brain: the neurophysics of EEG. 2*. New York: Oxford University Press.

Pavlov, A., Makarov, V. A., Makarova, J., & Panetsos, F. (2007). Sorting of neural spikes: when wavelet based methods outperform principal component analysis. *Natural Computing, 6*, 269–281.

Pettersen, K. H., & Einevoll, G. T. (2008). Amplitude variability and extracellular low-pass filtering of neuronal spikes. *Biophysical Journal, 94*, 784–802.

Ranck, J. B., Jr. (1973). Studies on single neurons in dorsal hippocampal formation and septum in unrestrained rats. I. Behavioral correlates and firing repertoires. *Experimental Neurology, 41*(2), 461–531.

Rudolph, M., Pelletier, J. G., Paré, D., & Destexhe, A. (2005). Characterization of synaptic conductances and integrative properties during electrically induced EEG-activated states in neocortical neurons *in vivo*. *Journal of Neurophysiology, 94*, 2805–2821.

Somogyi, P., & Klausberger, T. (2005). Defined types of cortical interneurone structure space and spike timing in the hippocampus. *Journal of Physiology, 562*, 9–26.

Spruston, N., & Johnston, D. (1992). Perforated patch-clamp analysis of the passive membrane properties of three classes of hippocampal neurons. *Journal of Neurophysiology, 67*, 508–529.

Tanskanen, J. M., Mikkonen, J. E., & Penttonen, M. (2005). Independent component analysis of neural populations from multielectrode field potential measurements. *Journal of Neuroscience Methods, 145*(1–2), 213–232.

Varona, P., Ibarz, J. M., López-Aguado, L., & Herreras, O. (2000). Macroscopic and subcellular factors shaping CA1 population spikes. *Journal of Neurophysiology, 83*, 2192–2208.